ORIGINAL ARTICLE

Influence of intermediate roll shifting on strip shape in a CVC-6 tandem cold mill based on a 3D multi-stand FE model

Lianjie Li[1] · Haibo Xie[1] · Tao Zhang[1] · Di Pan[1] · Xingsheng Li[2] · Fenghua Chen[1] · Tianwu Liu[3] · Xu Liu[3] · Hongqiang Liu[3] · Li Sun[3] · Zhengyi Jiang[1]

Abstract

Intermediate roll shifting (IRS) is widely used for improving the strip shape in the six-high tandem cold mill, but most related studies are limited to a single stand. To fill the knowledge gap, a three-dimensional (3D) multi-stand elastic–plastic finite element (FE) model was developed for a continuously variable crown (CVC)-6 tandem cold mill using data transfer, which was then validated by industrial experimental results. Based on this FE model, the effects of the IRS on the strip crown, strip flatness, loaded roll gap profile and contact normal stress between rolls at each stand were quantitatively analysed. The results show that from Stand 1 (S1) to Stand 5 (S5), the regulation ability of the IRS on the strip crown shows a decreasing trend, which depends on the strip plastic rigidity; in contrast, the regulation ability on the quadratic flatness experiences an obvious increase from S1 to Stand 4 (S4), then a drop at S5, while the IRS exerts little effect on the quartic flatness and quartic crown of the loaded roll gap. Moreover, the most uniform distribution of contact normal stress emerges at different IRSs from S1 to S5. These findings can contribute to a better understanding of the role of the IRS in controlling the strip shape during tandem cold rolling (TCR).

Keywords Intermediate roll shifting · Strip shape · 3D multi-stand FE model · CVC-6 tandem cold rolling

1 Introduction

In the strip rolling process, the technical key for strip shape control is how to achieve an even loaded roll gap profile. This is because the uneven loaded roll gap profile leads to nonuniform deformation and residual stress of the rolled strip, resulting in undesirable strip shape [1, 2]. To make the loaded roll gap profile more uniform, many control approaches such as different roll stack layouts, process technologies and roll contours, as summarised in Table 1, have been developed in recent decades. Among these methods, due to the advantages that include sample structure, large crown adjustment range and high flexibility [3], the intermediate roll shifting with the CVC contour has been widely applied in many six-high TCR production lines in the world. Figure 1 presents the schematic layout of a CVC-6 mill, which is equipped with the IRS, intermediate roll bending (IRB) and work roll bending (WRB). Figure 2 illustrates the crown adjustment of the roll gap by roll axial shifting with the CVC contour. It indicates that the roll gap crown varies from positive to negative when the roll shifts axially from negative to positive.

Since the CVC contour was invented by the SMS group in the 1980s [11], it has attracted enormous interest from many researchers and engineers. Jiang et al. [15] deduced a design principle for a three-order CVC curve and designed a five-order CVC curve with the capacity to control quarter buckle. Lu et al. [16] designed a three-order CVC curve with consideration given to minimising the axial force on the WR. Xu et al. [17] built a mathematical model for the CVC-Plus WR curve. Wang et al. [18] performed a comparison among the

✉ Tianwu Liu
liutianwu@hbisco.com

✉ Zhengyi Jiang
jiang@uow.edu.au

Lianjie Li
ll940@uowmail.edu.au

1 School of Mechanical, Materials, Mechatronic and Biomedical Engineering, Faculty of Engineering and Information Sciences, University of Wollongong, Wollongong, NSW 2522, Australia

2 Graduate School of Engineering, Osaka University, Osaka 565-0871, Japan

3 HBIS Group Technology Research Institute, Shijiazhuang, Hebei 050023, People's Republic of China

Table 1 Strip shape control approaches

Control approaches	Types
Roll stack layouts	Six-high mill [4, 5], X-type six-high mill [6], 12-high cluster mill [7], Sendzimir mill [8], pair cross [9]
Process technologies	Roll bending, roll shifting, roll stepped cooling [10]
Roll contours	CVC [11], varying contact back-up roll [12], SmartCrown [13], taper work roll [14]

SmartCrown, CVC-Plus and CVC in a six-high cold mill and found that the CVC-Plus has the best quadratic crown adjusting ability, while the SmartCrown is the most capable of adjusting quartic crown. Ding et al. [19] proposed a sextic CVC WR curve to improve the plate crown in the plate rolling process.

Apart from the above analysis and design for the CVC contour by theoretical calculation, the effects of the IRS on the strip shape have also been extensively studied using the finite element method. Sun et al. [20] analysed the effects of the IRS on the elastic deformation of rolls in a CVC-6 mill using a 3D elastic–plastic FE model. Linghu et al. [21] studied the effects of the IRS on the strip crown, edge drop and contact normal stress between rolls in a CVC-6 mill via a 3D elastic–plastic FE model. Li et al. [22] calculated the efficiency function of the IRS in a CVC-6 mill based on a 3D elastic–plastic FE model and proposed a segmented CVC contour to improve the edge and centre coupled wave. Wang et al. [23, 24] developed a 3D elastic–plastic FE model for a six high Universal Crown mill

and studied the effects of the IRS on the strip crown, strip flatness, contact normal stress between rolls, elastic deflection of rolls, rolling pressure, vertical and transverse rigidity. Using a similar FE model, Wang et al. [18] also discussed the effects of the IRS on the contact normal stress between rolls, strip crown and flatness under different strip widths in a SmartCrown-6 mill. However, the above studies are all limited to a single-stand FE model, so the influence of the previous stand on the following stand was neglected; more precisely, the work hardening effect caused by plastic deformation accumulation in multi-pass cold rolling has not been considered, which results in a considerable error. Wang et al. [25] studied the effect of the work roll shifting on the strip crown and its influence on the following stand considering the work hardening effect in a six-high tandem cold mill. However, the simulation was limited to the first two stands. In our previous studies [26, 27], a novel 3D elastic–plastic multi-stand FE model has been proposed for the TCR, in which the strip crown and equivalent plastic strain were transferred from one stand to the neighbouring stand, thus making it available for studying the effects of the IRS on the strip shape at each pass during the TCR.

In this study, the theoretical analysis of the adjustment ability of the CVC contour on the roll gap crown was conducted at first, and then a 3D multi-stand elastic–plastic FE model was established for a CVC-6 tandem cold mill using a segmentation modelling strategy and data transfer technology. Following that, the effects of the IRS on the strip crown, strip flatness, loaded roll gap and contact normal stress between rolls at each stand from S1 to S5 were revealed and discussed. The novelty of this study is that the present study expands the research on the influence of the IRS on the strip shape from a single stand to multi stands and determines the relationship between the regulation ability of the IRS on the strip crown and the strip plastic rigidity. This work can provide valuable guidelines for the IRS setting in practical strip shape control.
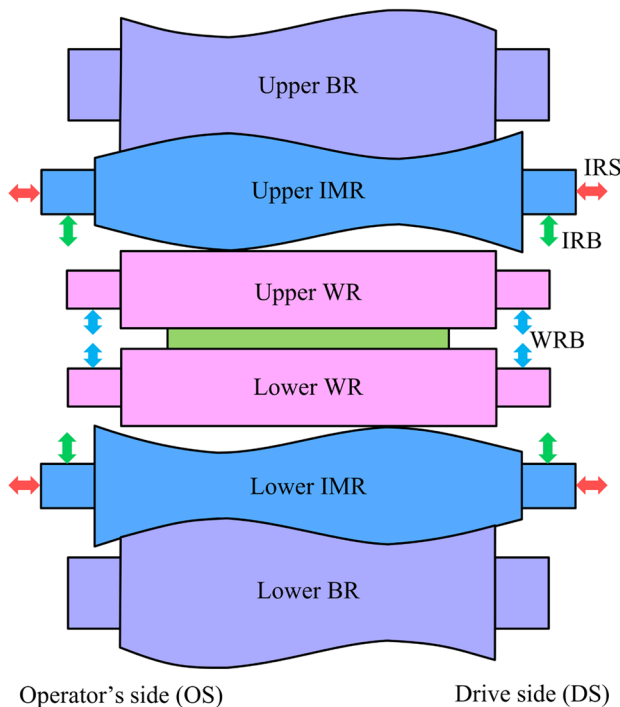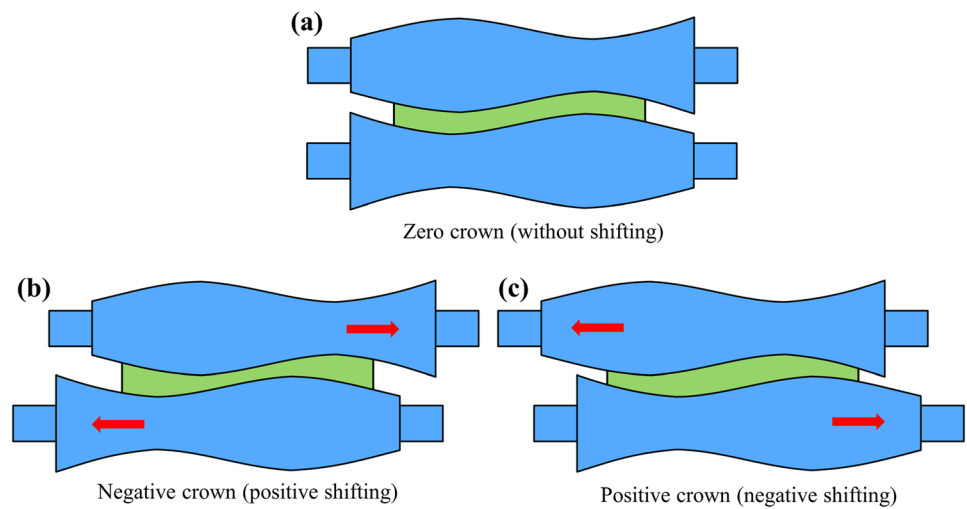
2 Analysis of the CVC contour

In the CVC-6 tandem cold mill, the WR contour was the conventional contour, and the contours of the IMR and BR were three-order CVC and reverse-CVC, respectively. According to the coordinate system of the CVC contour, as shown in Fig. 3, the three-order CVC curve can be modelled by Eq. (1).

Fig. 1 Two-dimensional schematic diagram of a CVC-6 mill. WR denotes the work roll; IMR denotes the intermediate roll; BR denotes the backup roll

Fig. 2 The crown variation of the roll gap induced by axial roll shifting with the CVC contour

(a)

Zero crown (without shifting)

(b)   (c)

Negative crown (positive shifting)   Positive crown (negative shifting)

$$R(x) = R_0 + a_1 x + a_2 x^2 + a_3 x^3 \quad (1)$$

where R_0 is the initial radius of IMR; a_1, a_2 and a_3 are the constant coefficients, listed in Table 2.

When the IMR was shifted laterally by s mm, the function of the upper IMR contour can be described by Eq. (2). According to the anti-symmetric layout of the upper and lower IMRs, the function of the lower IMR contour can be expressed as Eq. (3).

$$R_U(x,s) = R_0 + a_1(x-s) + a_2(x-s)^2 + a_3(x-s)^3 \quad (2)$$

$$R_L(x,s) = R_0 + a_1(L-x-s) + a_2(L-x-s)^2 + a_3(L-x-s)^3 \quad (3)$$

where s is the axial shifting value, varying from -200 to 200 mm; L is the barrel length of the IMR, 2580 mm here.

Ignoring the influence of the small WR crown, the function of the unloaded roll gap can be obtained as Eq. (4).

$$G(x,s) = D + H - R_U(x,s) - R_L(x,s) \quad (4)$$

where D is the diameter of the IMR and H is the roll gap.

Substituting Eqs. (2) and (3) into Eq. (4), Eq. (4) can be rewritten into Eq. (5).

$$G(x,s) = (D + H - 2R_0) - a_1(L - 2s) \\ - a_2\big((x-s)^2 + (L-x-s)^2\big) \\ - a_3\big((x-s)^3 + (L-x-s)^3\big) \quad (5)$$

According to Eq. (5), the equivalent crown of the unloaded roll gap can be deduced, as shown in Eq. (6). From Eq. (6), it can be found that the $C_W(x,s)$ has a linear relationship with s. Specifically, it can be observed from Fig. 4 that the $C_W(x,s)$ decreases linearly with the increase in the IMR axial shifting.

$$C_W(x,s) = G(2/L,s) - G(0,s) = \frac{1}{2}a_2 L^2 + \frac{3}{4}a_3 L^3 - \frac{3}{2}a_3 L^2 s \quad (6)$$

The cross-sectional profile of the unloaded roll gap is assumed to be symmetrical about the rolling centre, which can be modelled as a quartic polynomial function. The quadratic and quartic components correspond to the quadratic and quartic crowns, respectively, as shown in Eqs. (7) and (8) [18]. From Eq. (7), it can be seen that the quadratic crown C_{W2} is the same as the $C_W(x,s)$. By contrast, the value of the quartic crown C_{W4} is zero, which means that
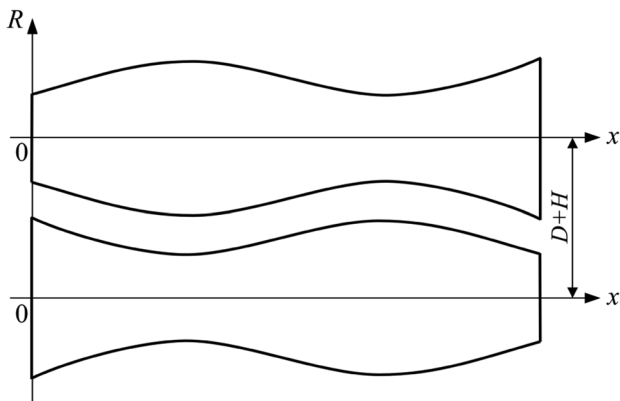

Fig. 3 The coordinate system of the CVC contour

Table 2 Coefficients of CVC contour

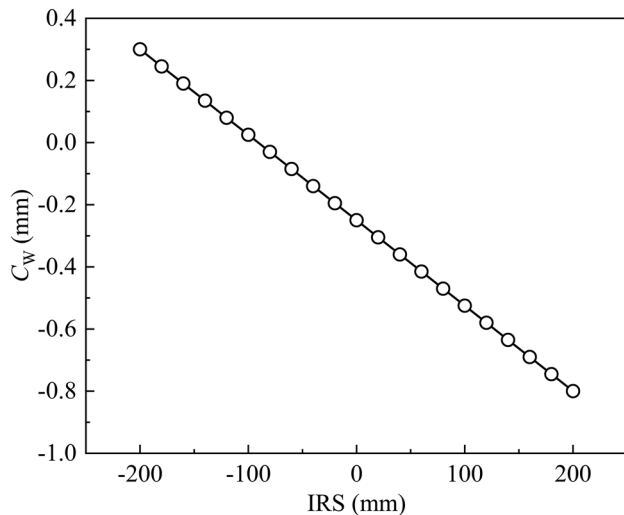| Coefficients	Value
a_1	0.141331E−02
a_2 (1/mm)	−0.114101E−05
a_3 (1/mm²)	0.275424E−09

Fig. 4 Equivalent crown C_W under different IRSs

the three-order CVC contour has no ability to regulate the quartic flatness.

$$C_{W2} = \frac{1}{2}a_2L^2 + \frac{3}{4}a_3L^3 - \frac{3}{2}a_3L^2s \qquad (7)$$

$$C_{W4} = 0 \qquad (8)$$

3 3D multi-stand FE model for the TCR

This section presents a 3D multi-stand elastic–plastic FE model for the TCR process developed based on the MSC Marc software. In addition, industrial experiments were carried out to validate the established FE model.

3.1 Modelling techniques

Figure 5a displays a 2180 mm CVC-6 tandem cold mill, which consists of five identical CVC-6 mills arranged in a line. If they are all modelled in one FE model, it will take millions of elements, resulting in high computation costs. Also, the strip elements will suffer severe distortion due to the substantial elongation generated by heavy reduction through five passes. To address this issue, the following modelling techniques were adopted.

1. The segmentation modelling strategy was utilised to divide the tandem cold mill into five independent stands (S1, S2, S3, S4 and S5), each of which was modelled as a separate FE model, as shown in Fig. 5b.
2. To integrate these individual FE models into a whole model, data transfer technologies were developed to transfer data between neighbouring stands. These tech-
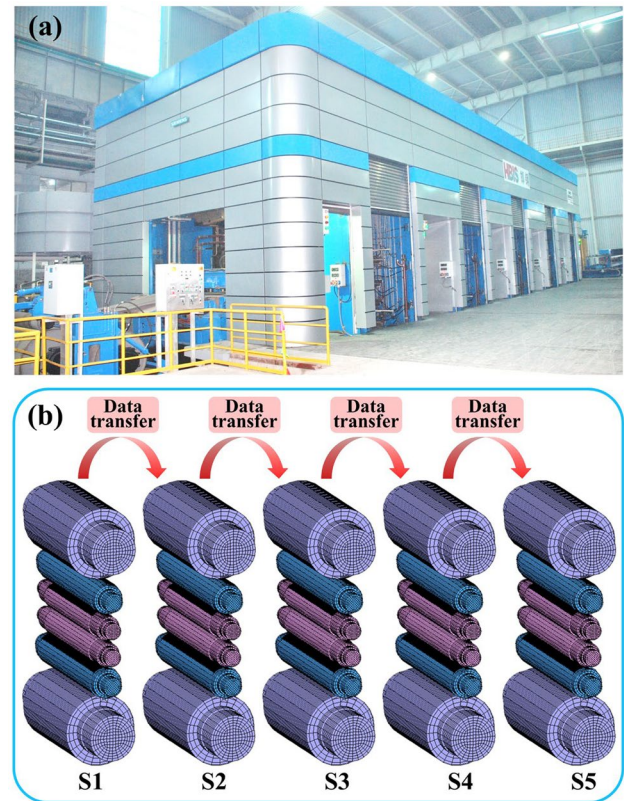

Fig. 5 **a** 2180 mm CVC-6 tandem cold mill; **b** 3D multi-stand FE model for the TCR process

nologies include transferring the strip crown via the Mentat commands in Marc and transferring the total equivalent plastic strain at the strip elements' integration points via the self-developed Elevar and Initpl subroutines.
3. To maintain the regularity of strip elements, the strip elements need to be remeshed after each pass, which was conducted during the data transfer process. During the element remeshing process, the number of new elements and nodes should be in accord with that of the deformed elements and nodes of the previous stand.

Furthermore, the five distinct FE models were calculated sequentially. The detailed modelling process and roll size parameters are presented in our previous studies [26, 27].

3.2 Material properties

In this model, the strip material was a kind of deep drawing steel named DC01. The WR, IMR and BR were made of Cr5 forged steel. The strip and rolls were characterised as elastic–plastic body and elastic bodies, respectively, and their physical properties are summarised in [27]. Taking into account the work hardening effect, rolling-tension tests were

conducted to determine the strip's static deformation resistance, which can be expressed by Eq. (9) [26].

$$\sigma_s = 365.54 + 208.1\varepsilon^{0.381} \qquad (9)$$

$$\varepsilon = \ln \frac{H}{h} \qquad (10)$$

where σ_s is the plastic deformation resistance; ε is the true strain, which can be expressed as Eq. (10); H and h are the strip entry and exit thickness, respectively.

3.3 Simulation conditions

Table 3 lists the process parameters of stands S1–S5. Nine different IRSs (−200 mm, −150 mm, −100 mm, −50 mm, 0 mm, 50 mm, 100 mm, 150 mm and 200 mm) were selected to develop the FE model from S1 to S5. The implicit algorithm based on the full Newton–Raphson method was used to solve the nonlinear equilibrium equations. Besides, the Coulomb bilinear friction model was adapted to define the rolling contact behaviour. Furthermore, every single FE model was meshed by the eight-node hexahedral elements (i.e. the element type 7 in Marc), with a total element number of 214,808. As shown in Fig. 6, there are four elements in the thickness direction; the strip was divided into three parts in the width direction, including two finely-meshed strip edge regions (100 mm in length) with an element length of 10 mm and a coarsely meshed strip central region with an element length of 13.56 mm, respectively; the element length is 0.9 mm in the rolling direction. To be closer to the actual situation, the tension was added to the strip head and tail. The computation was carried out using a workstation powered by an Intel Xeon E5-2667 v3 CPU and 64 GB of RAM.

3.4 Validation of the 3D multi-stand FE model

To verify the generality of the developed FE model, two industrial trial cases with different specifications were conducted on the 2180 mm TCR mill. According to previous
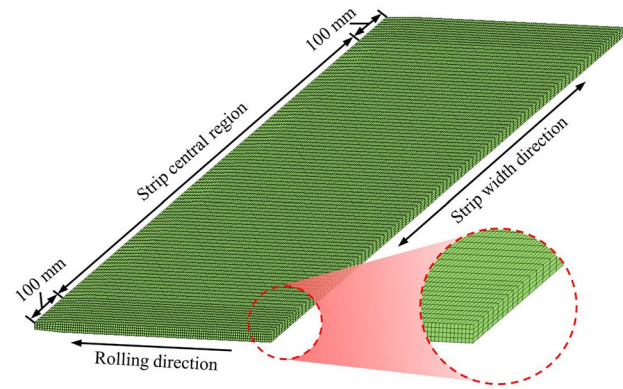

Fig. 6 Element meshing of the strip

studies [2, 18], Wang et al. verified the FE model by comparing the experimental and simulated rolling forces. In this study, the experimental and simulated rolling forces are compared, as summarised in Tables 4 and 5. It is noted that the experimental rolling force was obtained from the PDA (process data acquisition) data. It is clear that the rolling force shows a downward trend from S1 to S5, which is due to the decrease in pass reduction [28, 29]. In addition, the simulated rolling force accords with the experimental value, with a relative error of less than 5%. Therefore, the developed multi-stand FE model is accurate and reliable.

4 Evaluation index of strip shape

In actual production, the strip shape quality is mainly evaluated in terms of the cross-sectional profile and flatness. They are assessed using a variety of indexes as follows.

4.1 Strip cross-sectional profile

The strip cross-sectional profile is displayed in Fig. 7. Here, the C_{40} (characteristic value of the strip crown) is

Table 3 Rolling process parameters

Stand	Entry thickness (mm)	Exit thickness (mm)	Entry tension (kN)	Exit tension (kN)	WRB (kN)	IMB (kN)	IRS (mm)	Rolling velocity (m/s)
S1	4.409	3.013	255	465	271	280		3.5
S2	3.013	1.927	465	330	270	273	−200, −150, −100, −50,	5.0
S3	1.927	1.343	330	245	309	302	0, 50, 100, 150, 200	7.5
S4	1.343	1.057	245	195	328	323		10.5
S5	1.057	1.000	195	40	220	225		14.5

Table 4 The rolling parameters of case 1 with the strip width of 1540 mm

Stand	Entry thickness (mm)	Exit thickness (mm)	Entry tension (kN)	Exit tension (kN)	WRB (kN)	IMB (kN)	IRS (mm)	Rolling velocity (m/s)	P_{exp} (kN)	P_{FEM} (kN)	Relative error (%)
S1	2.691	1.941	223	355	245	240	5	3.5	12,674	13,183	4.02
S2	1.941	1.332	355	274	260	240	5	4.7	12,561	12,712	1.20
S3	1.332	0.996	274	215	260	355	30	6.9	10,750	11,025	2.56
S4	0.996	0.803	215	182	280	274	30	9.1	10,114	10,277	1.61
S5	0.803	0.8.00	182	38.5	225	328	28	11.7	7471	7662	2.56

P_{exp} experimental rolling force, P_{FEM} simulated rolling force

adopted as the main index to evaluate the quality of the strip cross-sectional profile, expressed as Eq. (11) [30].

$$C_{40} = \frac{\left(h_c - h'_d\right) + \left(h_c - h''_d\right)}{2} \quad (11)$$

where h_c is the centre thickness; h'_d and h''_d are the thickness at 40 mm from the edge (DS side and OS side, respectively).

4.2 Strip flatness

According to the bucking position in the strip width direction, the flatness defect can be divided into the centre wave, edge wave, quarter wave and edge-centre coupled wave (see Fig. 8). Buckling takes place during the strip rolling process due to the strip fibres' nonuniform elongation, which is caused by the uneven reduction along the strip width direction under the unevenly-loaded roll gap. If the rolled strip sample is sliced longitudinally into several narrow fibres, the fibres will contract or stretch elastically in response to the release of residual tension. Thus, the strip flatness can be represented by the relative difference in the lengths of these fibres, expressed as Eq. (12) [3]. The flatness can be written as Eq. (13) [3].

$$\varepsilon_V(x) = \frac{L(x) - \overline{L}}{\overline{L}} \quad (12)$$

where $\varepsilon_v(x)$ is the relative difference in the lengths of fibres at location x; $L(x)$ is the length of strip fibre (60 elements here) at location x; $\overline{L}$ is the average length of the strip fibres (60 elements here).

$$I(x) = \varepsilon_V(x) \times 10^5 = \frac{L(x) - \overline{L}}{\overline{L}} \times 10^5 \quad (13)$$

where $I(x)$ is the flatness at location x (in IU).

In the actual production, the strip flatness is measured through the tensile stress based on the shape roll, which can be expressed as the difference between the front tensile stress and the average tensile stress, as shown in Eq. (14) [31].

$$\Delta\sigma(x) = \sigma(x) - \overline{\sigma} \quad (14)$$

where $\sigma(x)$ is the front tensile stress at location x; $\overline{\sigma}$ is the average tensile stress.

The tensile stress difference $\Delta\sigma(x)$ can also be described as Eq. (15) [3]. From Eq. (15), it can be confirmed that the $\varepsilon_v(x)$ should be the elastic deformation of the fibres, not the plastic deformation. Therefore, during the postprocessing of the FE model, the elastic deformation of 60 elements (in the stable rolling stage) in the rolling direction was used to evaluate the flatness according to Eq. (13).

$$\Delta\sigma(x) = E\varepsilon_V(x) \quad (15)$$

where E is the elastic modulus.

A quartic polynomial can be employed to fit the flatness curve, as Eq. (16), which can be reformulated using Chebyshev polynomials [32, 33] as Eq. (17).

$$I(x) = a_0 + a_1 x + a_2 x^2 + a_3 x^3 + a_4 x^4 \quad (16)$$

where a_0, a_1, a_2, a_3, a_4 are the coefficients; x is the normalised width, from -1 to 1.

$$I(x) = -\frac{1}{2}xFlt_1 - \frac{1}{2}\left(2x^2 - 1\right)Flt_2 \\ - \frac{1}{2}\left(4x^3 - 3x\right)Flt_3 - \frac{1}{2}\left(8x^4 - 8x^2 + 1\right)Flt_4 + \Delta \quad (17)$$

where Flt_1 is the first flatness; Flt_2 is the quadratic flatness; Flt_3 is the cubic flatness; and Flt_4 is the quartic flatness; Flt_2 and Flt_4 can be expressed by Eqs. (18) and (19), respectively; Δ is the error.

$$Flt_2 = -a_2 - a_4 \quad (18)$$

$$Flt_4 = -\frac{1}{4}a_4 \quad (19)$$

From Eqs. (17) to (19), it can be determined that when $Flt_2 > 0$, it is the centre wave, whereas when $Flt_2 < 0$, it is the edge wave; when $Flt_4 > 0$, it is the quarter wave,

Table 5 The rolling parameters of case 2 with the strip width of 1285 mm

Stand	Entry thickness (mm)	Exit thickness (mm)	Entry tension (kN)	Exit tension (kN)	WRB (kN)	IMB (kN)	IRS (mm)	Rolling velocity (m/s)	P_{exp} (kN)	P_{FEM} (kN)	Relative error (%)
S1	2.693	2.023	186	295	244	272	25	4.0	10,460	10,793	3.18
S2	2.023	1.456	295	238	239	220	25	5.3	10,421	10,612	1.83
S3	1.456	1.133	238	194	239	243	60	7.3	9345	9425	0.85
S4	1.133	0.933	194	166	271	270	60	9.4	8904	8867	−0.41
S5	0.933	0.923	166	37	198	255	128	11.6	6468	6562	1.46
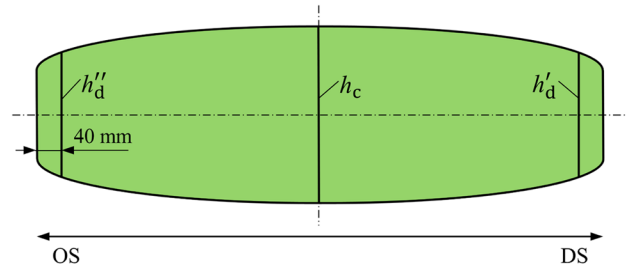
Fig. 7 Sketch map of strip cross-sectional profile

whereas when $Flt_4 < 0$, it is the edge-centre coupled wave [26].

4.3 Evaluation index of the effect of the IRS on the strip shape

To quantitatively evaluate the effect of the IRS on the strip crown, the efficiency factor K_C is introduced by Eq. (20).

$$K_C = \frac{\Delta C_{40}}{\Delta IRS} \tag{20}$$

where ΔC_{40} denotes the variation of C_{40}; ΔIRS denotes the variation of the IRS.

To quantify the effect of the IRS on the strip flatness, the efficiency factor K_F is proposed by Eq. (21).

$$K_F = \frac{\Delta Flt}{\Delta IRS} \tag{21}$$

where ΔFlt is the variation of the strip flatness.

To quantify the influence of the IRS on the crown of the loaded roll gap profile, the efficiency factor K_W is indicated by Eq. (22).
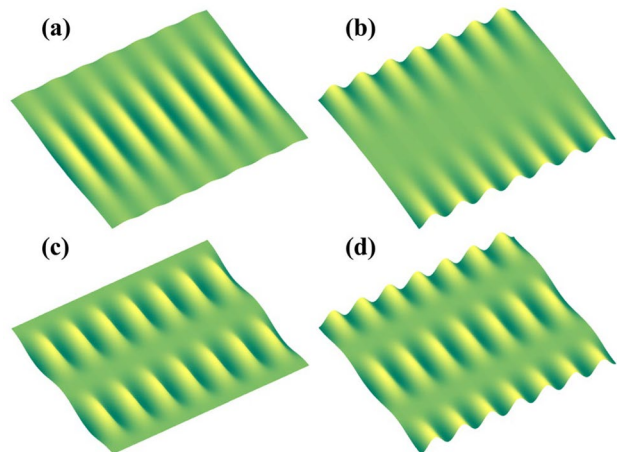
Fig. 8 Flatness types: **a** centre wave; **b** edge wave; **c** quarter wave; **d** edge-centre coupled wave
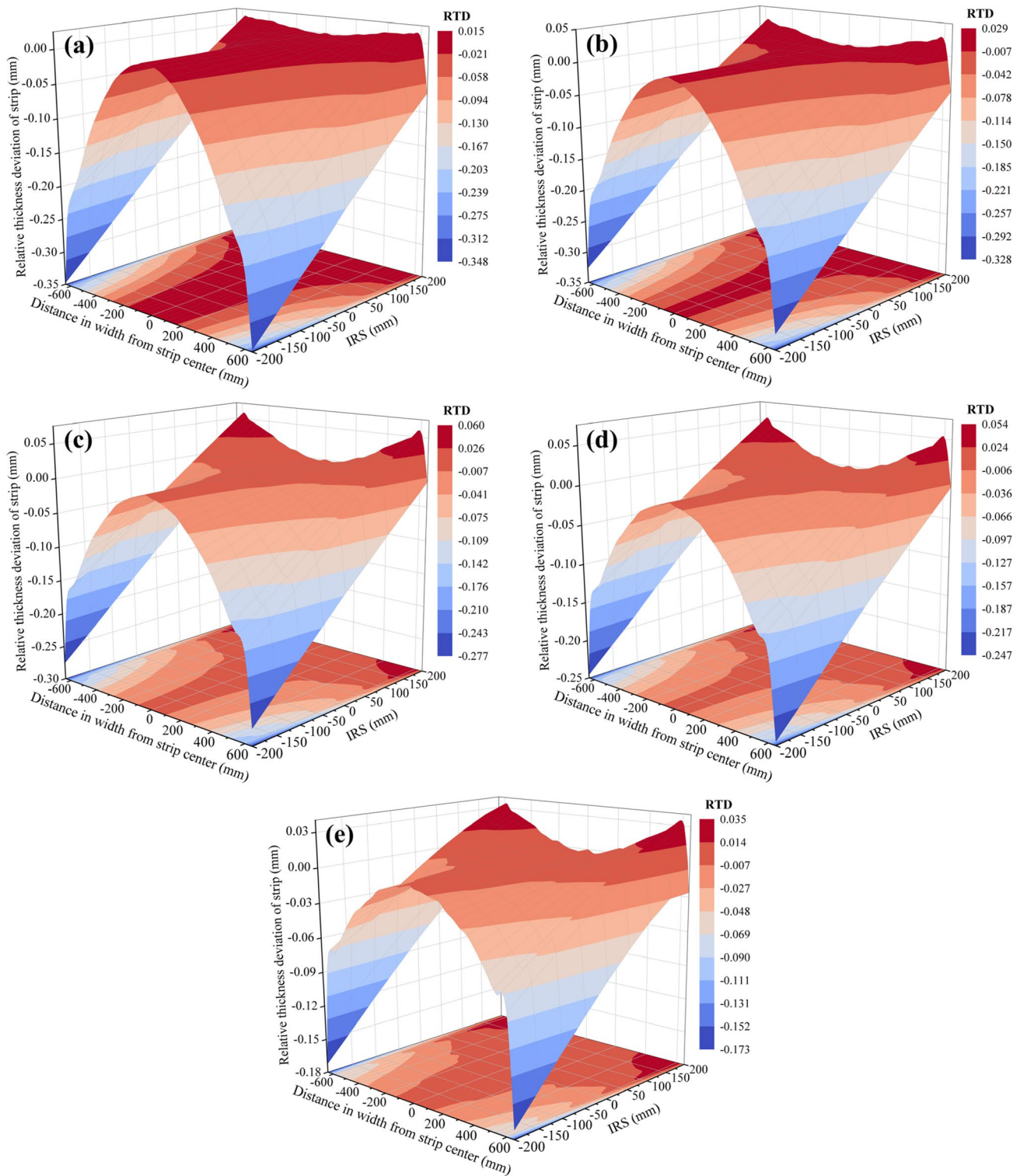
Fig. 9 The strip's RTD under different IRSs: **a** S1; **b** S2; **c** S3; **d** S4; **e** S5

$$K_{W} = \frac{\Delta C_{W}}{\Delta IRS} \tag{22}$$

where ΔC_{W} is the crown variation of the loaded roll gap profile.

Due to different roll contours of WR, IMR and BR, as well as the elastic deflection and flattening deformation of the roll stack, the contact normal stress between rolls is unevenly distributed, which has a direct effect on the roll wear. To evaluate the nonuniform distribution degree, a

nonuniform coefficient β is defined as Eq. (23) [21]. The larger β is, the more nonuniformly contact normal stress is distributed.

$$\beta = \frac{p_{max}}{p_{ave}} \tag{23}$$

where p_{max} is the maximum contact normal stress; p_{ave} is the average contact normal stress.

5 Results

5.1 Effects of the IRS on the strip crown

Figure 9 illustrates the relative thickness deviation (RTD) of the strip under various IRSs from S1 to S5. As seen in Fig. 9, the RTD is distributed non-uniformly along the strip width direction; specifically, the RTD at the strip edge is significantly greater than that in the central region, forming the so-called edge drop. With the increase in the IRS from −200 to 200 mm, the shape of the RTD changes from a 'hill' to a 'valley'. Furthermore, from S1 to S5, the range of the RTD sees a downward trend on the whole.

Figure 10 presents the efficiency curves of the IRS on the strip crown from S1 to S5. It can be seen from Fig. 10 that all the curves exhibit a linearly declining trend with an increase in the IRS, although with varying slopes. To be more precise, when the IRS increases from −200 to 200 mm, the strip crown C_{40} of S1 decreases steeply from 230.2 to −11.3 μm; similarly, the C_{40} of S2 drops from 210.3 to −26.9 μm. When it comes to S3 and S4, with the increase in the IRS from −200 to 200 mm, the C_{40} of S3 sees a drop from 165.8 to −59.8 μm, while the C_{40} of S4 also experiences a relatively slight decrease from 137.0 to −53.6 μm; in contrast, the C_{40} of S5 undergoes the smallest decrease from 71.6 to −34.3 μm.
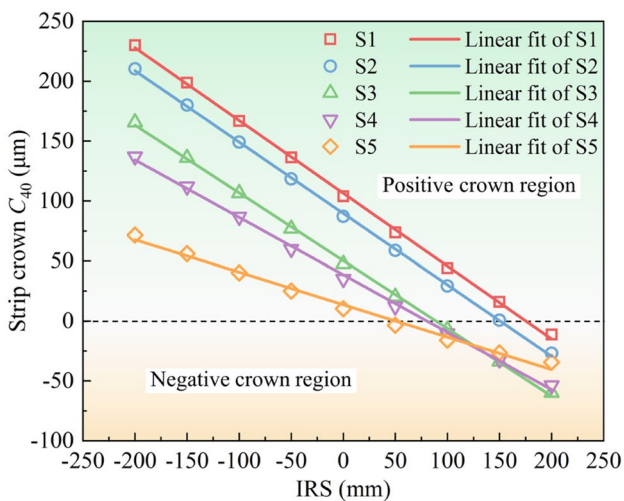
The K_C can be determined by fitting the efficiency curves from Fig. 10 according to Eq. (20), namely the slopes, as seen in Fig. 11. It can be observed from Fig. 11 that, from S1 to S3, the absolute value of K_C decreases slowly from 0.608 to 0.565 μm/mm, and then decreases sharply to 0.271 μm/mm at S5. This demonstrates that the influence of the IRS on the strip crown decreases gradually from S1 to S3, while decreasing dramatically from S3 to S5.

5.2 Effects of the IRS on the strip flatness

Figure 12 displays the strip flatness under various IRSs from S1 to S5. As shown in Fig. 12, the flatness along the strip width direction changes drastically with the variation of the IRS; opposite to the RTD, the shape of the flatness changes from a 'valley' to a 'hill' (i.e. from 'edge wave' to 'centre wave'). To quantify the variation of the flatness, the flatness curves can be decomposed into Flt_2 and Flt_4 according to Eq. (17), as displayed in Fig. 13. From Fig. 13a, it can be found that when the IRS increases from −200 to 200 mm, the Flt_2 increases linearly from −7.41 to 1.92 IU, which indicates that the quadratic flatness changes from the edge wave to the centre wave. The Flt_2 of stands S2-S5 all show a similar trend as that of S1.

Compared with Flt_2, the Flt_4 under different IRSs shows an obviously nonlinear trend, as seen in Fig. 13b. Specifically, when the IRS increases from −200 to 200 mm, the Flt_4 of S1 decreases from 0.24 to 0.05 IU, which suggests that the type of quartic flatness is the quarter wave, with decreasing intensity. By contrast, with an increase in the IRS from −200 to −100 mm, the Flt_4 of S2 increases
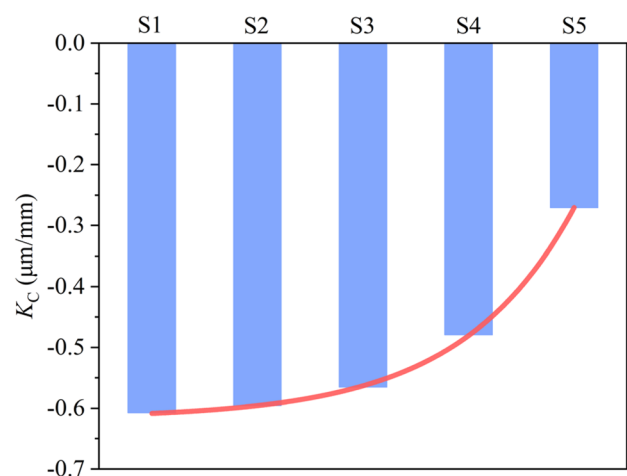

Fig. 10 The efficiency curves of the IRS on the strip crown

Fig. 11 The efficiency factor of the IRS on strip crown from S1 to S5
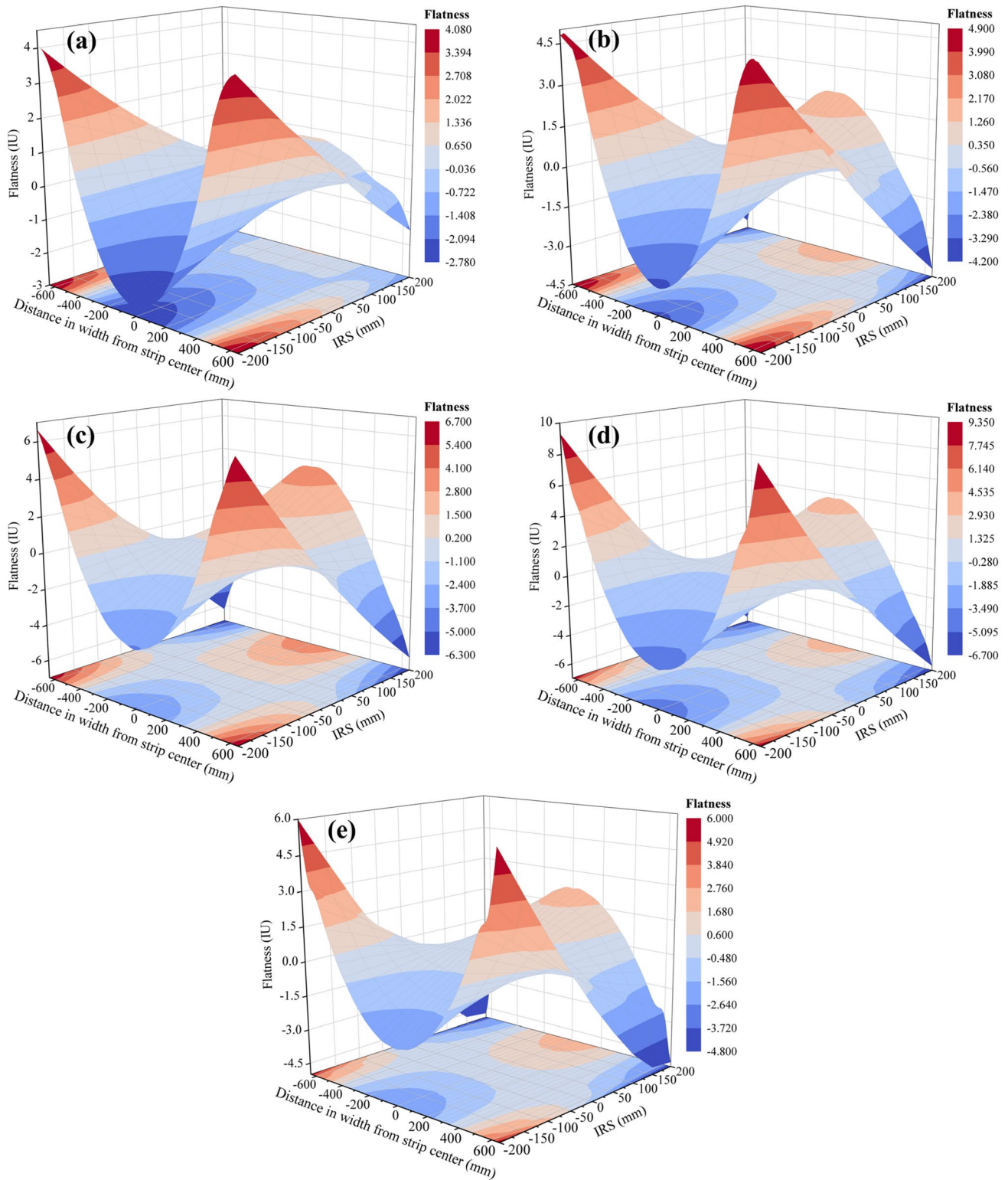
Fig. 12 Strip flatness under different IRSs: **a** S1; **b** S2; **c** S3; **d** S4; **e** S5

slowly from 0.45 to 0.52 IU, and then decreases gradually to 0.23 IU when the IRS increases to 200 mm. This suggests that the quarter wave appears, but with the peak intensity at −100 mm. When it comes to S3, the Flt_4 first experiences an increase from −0.25 to 0.10 IU when the IRS increases from −200 to 0 mm, and then drops to −0.21
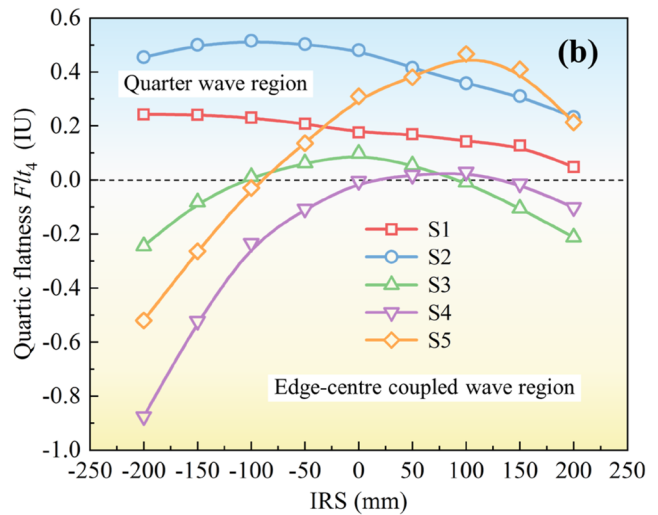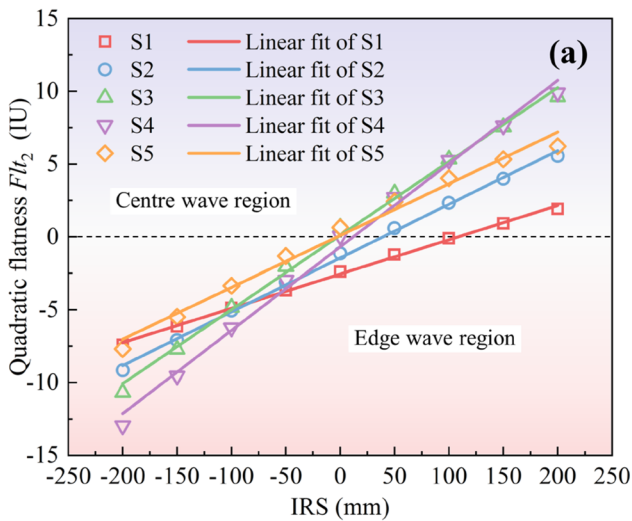
Fig. 13 The efficiency curves of the IRS on the Flt_2 (**a**) and Flt_4 (**b**)

IU when the IRS increases to 200 mm. This means that the quartic flatness evolves from the edge-centre coupled wave to the quarter wave, and then changes to the edge-centre coupled wave. The Flt_4 of S4 exhibits a similar trend as that of S3, but with the peak value at 100 mm. In comparison, the Flt_4 of S5 sees a dramatic increase from −0.52 to 0.47 IU when the IRS increases from −200 to 100 mm, and then undergoes a slight drop from 0.47 to 0.21 IU when the IRS increases from 100 to 200 mm. This implies that the quartic flatness evolves from edge-centre coupled wave to quarter wave, while the intensity of the quarter wave peaks at 100 mm.

The efficiency factor K_F of Flt_2 and Flt_4 from S1 to S5 are compared in Fig. 14. It can be observed from Fig. 14 that the K_F of Flt_2 is much greater than that of Flt_4, which indicates that the effect of the IRS on the quadratic flatness is far larger than that on the quartic flatness. In addition, from S1 to S4, the K_F of Flt_2 increases steadily from 0.023 to 0.057 IU/mm, and then decreases to 0.035 IU/mm at S5. This demonstrates that the influence of the IRS on the quadratic flatness rises substantially from S1 to S4, and then falls at S5. Comparatively, the K_F of Flt_4 is close to zero, negative at S1 and S2, but positive at S4 and S5. This means that the effect of the IRS on the quartic flatness is small and nonstable. This phenomenon will be discussed in the following part.

5.3 Effects of the IRS on the loaded roll gap profile

For the CVC-6 tandem cold mill here, the IRS can efficiently change the crown of the loaded roll gap profile, as shown in Fig. 15. It can be seen that when the IRS increases from −200 to 200 mm, the crown of the loaded roll gap profile decreases from positive to negative at each

stand, and the range of the loaded roll gap profile shows a downward trend from S1 to S5.

5.4 Effects of the IRS on the contact normal stress between rolls

Figure 16 compares the contact normal stress between the WR and IMR under various IRSs from S1 to S5. It is apparent that the contact normal stress along the WR width direction shows 'S' in shape, which accords with the shape of the CVC contour of IMR. With an increase in the IRS, the contact normal stress increases in the central region, but decreases at both WR edges.
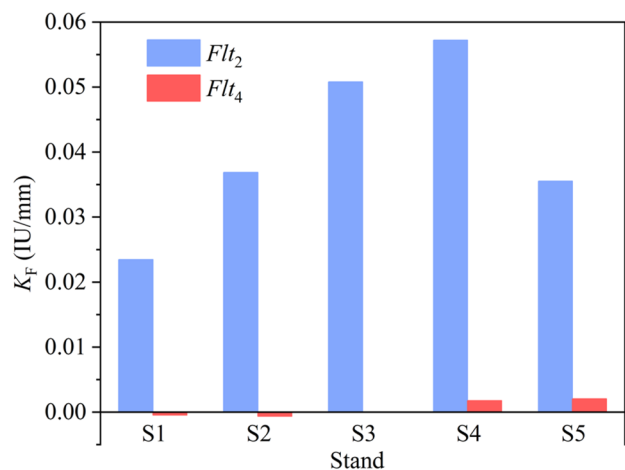

Fig. 14 The efficiency factors of the IRS on the strip flatness from S1 to S5
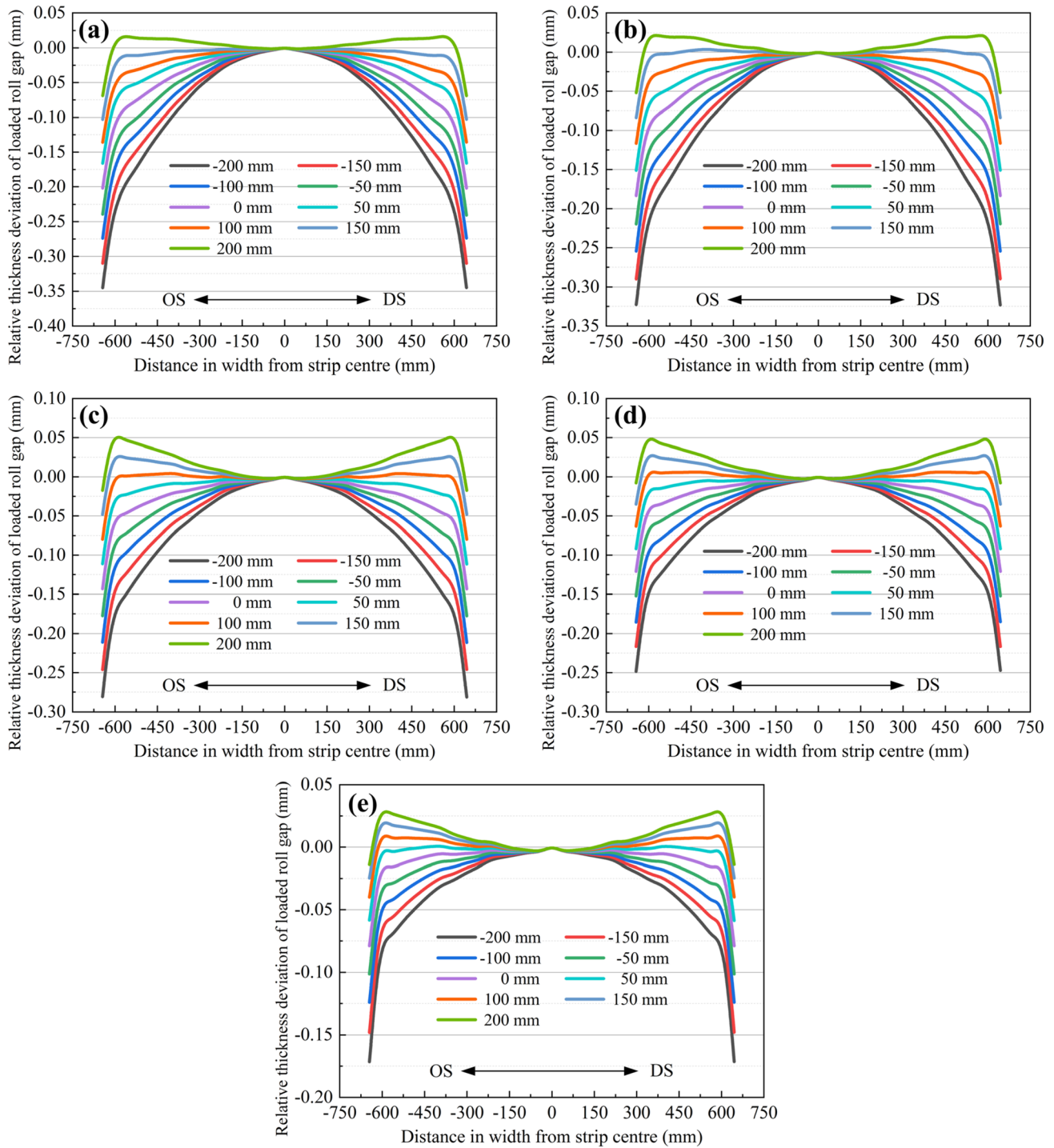
Fig. 15 The loaded roll gap profiles under different IRSs: **a** S1; **b** S2; **c** S3; **d** S4; **e** S5

The β_{WI} (nonuniform coefficient of the contact normal stress between the WR and IMR) under various IRSs from S1 to S5 is compared in Fig. 17. It can be seen from Fig. 17 that the β_{WI} shows an upward trend from S1 to S5 when it comes to the same IRS, while the β_{WI} varies nonlinearly with the IRS at each stand. Specifically, as for S1, the β_{WI}

first decreases gradually from 1.41 to 1.30 when the IRS increases from −200 to −50 mm, then continuously rises to 1.43 when the IRS increases to 200 mm. The β_{WI} at S2 has a similar pattern as that of S1. In comparison, the β_{WI} at S3 first sees a decrease from 1.50 to 1.35 when the IRS increases from −200 to 0 mm, then experiences an increase
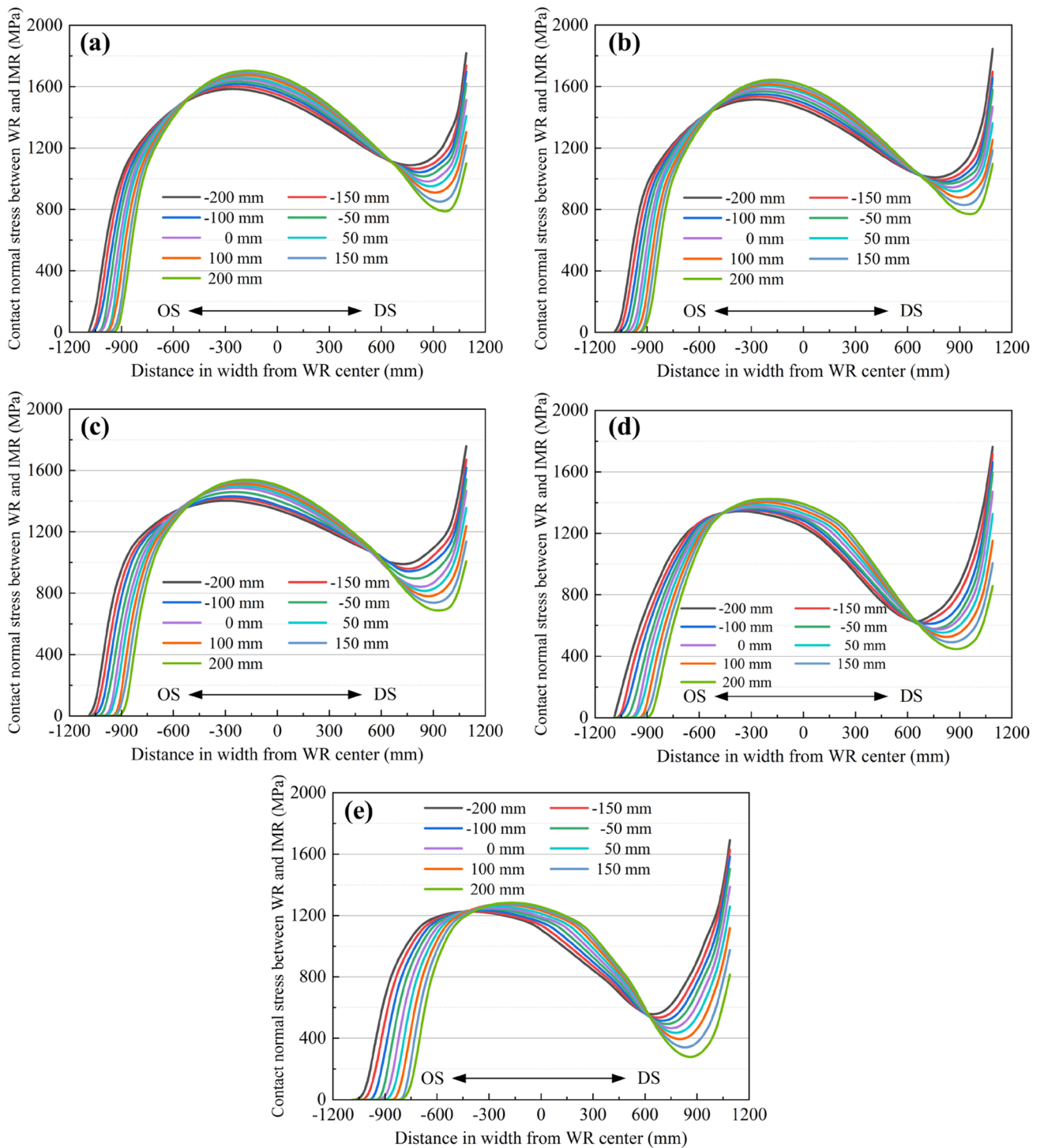
Fig. 16 Contact normal stress between the WR and IMR under different IRSs: **a** S1; **b** S2; **c** S3; **d** S4; **e** S5

to 1.48 when the IRS increases continuously to 200 mm. As for S4, there is a fall in β_{WI} from 1.74 to 1.49 when the IRS increases from −200 to 50 mm, and a rise in β_{WI} from 1.49 to 1.61 when the IRS increases from 50 to 200 mm. The β_{WI} at S5 follows a similar pattern as that of S4.

Figure 18 presents the contact normal stress between the IMR and BR under various IRSs from S1 to S5. It can be observed from Fig. 18 that when the IRS increases from −200 to 200 mm, the shape of contact normal stress along the BR width direction evolves from a 'saddle' to a 'hill'.
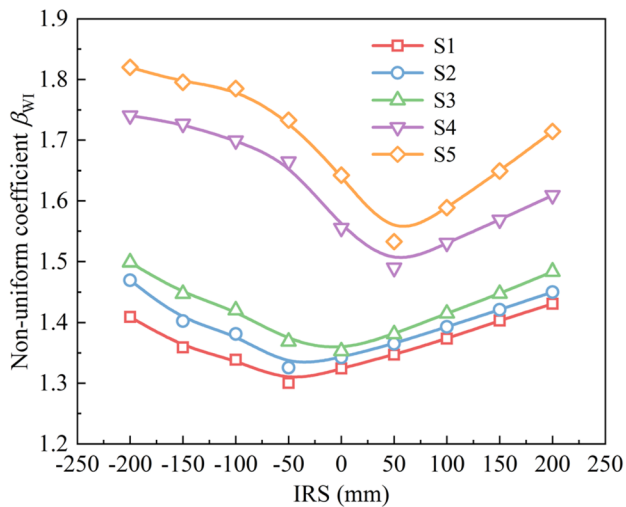
Fig. 17 The nonuniform coefficient β_{WI} under different IRSs from S1 to S5

In other words, the stress increases obviously in the central region, while it decreases significantly at both BR edges. This is similar to the variation of contact normal stress between the WR and IMR.

The β_{IB} (nonuniform coefficient of the contact normal stress between the IMR and BR) under various IRSs from S1 to S5 is shown in Fig. 19. As illustrated in Fig. 19, the β_{IB} shows an increasing trend at the same IRS from S1 to S5, except that the β_{IB} remains stable when the IRS ranges from −100 to 50 mm at stands S1–S4. Furthermore, the β_{IB} has a nonlinear relationship with the IRS. More precisely, the β_{IB} at S1 first decreases slightly from 1.12 to 1.07 when the IRS increases from −200 to −150 mm, but then increases steadily to 1.31 when the IRS increases to 200 mm. The β_{IB} at S2 and S5 has a similar trend as that of S1, except that the value at S5 is much larger than that at S1 and S2. By contrast, the β_{IB} undergoes a small drop from 1.15 to 1.08 when the IRS increases from −200 to −100 mm, but it sees a large increase from 1.08 to 1.35 when the IRS increases from −100 to 200 mm. S4 exhibits a similar tendency to S3.

6 Discussions

6.1 Relationship between the efficiency factor K_C and strip plastic rigidity

From Fig. 11, it can be seen that the value of K_C shows an increasing trend from S1 to S5, which is in good agreement with previous studies [31]. This trend is similar to that of the strip plastic rigidity Q calculated in our previous research [26], as shown in Fig. 20a. It can be observed that K_C is in near accordance with Q at each stand. Given the almost same mill

rigidity at each stand, K_C is dependent on Q. This is to say, K_C is related to the deformation resistance of the strip influenced by the work hardening effect.

To further study the relationship between K_C and Q, the curve of K_C versus Q is drawn in Fig. 20b. As illustrated in Fig. 20b, K_C increases nonlinearly with Q, which can be well described by an exponential function curve, as expressed in Eq. (24). This mathematical model provides a quantitative relationship instead of engineers' experience to predict the K_C at each stand. This offers a valuable reference for setting up the strip crown control model in terms of the IRS in the TCR.

$$K_C = -0.1258 - 0.52405 * \exp(-2.2749E - 5 * Q) \quad (24)$$

where Q denotes the strip plastic rigidity.

6.2 Relationship between the loaded roll gap profile and strip shape

The curves of the loaded roll gap profile (in Fig. 15) can be decomposed into the quadratic crown C_{W2} and quartic crown C_{W4}, as displayed in Fig. 21. From Fig. 21a, it can be observed that the C_{W2} decreases linearly with the increase in the IRS, but with different slopes. This is in line with the variation of C_{40} in Fig. 10, but contrary to the variation of Flt_2 in Fig. 13a. By contrast, it can be found from Fig. 21b that the C_{W4} varies nonlinearly with the IRS. More precisely, when the IRS increases from −200 to 200 mm, the C_{W4} of S1 and S2 shows an upward trend, while the C_{W4} of S4 and S5 displays a downward trend, whereas the C_{W4} of S3 fluctuates slightly at 30 μm. This tendency is opposite to the variation of Flt_4 in Fig. 13b.

Figure 22 compares the K_W of C_{W2} and C_{W4} from S1 to S5. It is apparent that the absolute value of K_W for the C_{W2} is much larger than that of the C_{W4}, which suggests that the IRS exerts a far greater effect on the C_{W2} than that on the C_{W4}. Besides, the value of K_W for the C_{W4} is close to zero and not stable; it is positive from S1 to S3, while it is negative at S4 and S5 (this is opposite to the value of K_F for the Flt_4 shown in Fig. 14). This is in line with the earlier analysis (in Sect. 2) that the three-order CVC contour is incapable of regulating the quartic flatness. Furthermore, the value of K_W for the C_{W2} is negative at each stand, and its absolute value shows a decreasing trend from 0.689 μm/mm at S1 to 0.356 μm/mm at S5. This agrees well with that of the K_C in Fig. 11, but this is contrary to that of K_F for the Flt_2 in Fig. 14. In summary, the C_{W2} of the loaded roll gap profile is similar to the C_{40}, but the C_{W2} and C_{W4} are contrary to the Flt_2 and Flt_4, respectively. This further demonstrates that the loaded roll gap profile controls the strip shape, including the strip cross-sectional profile and flatness.
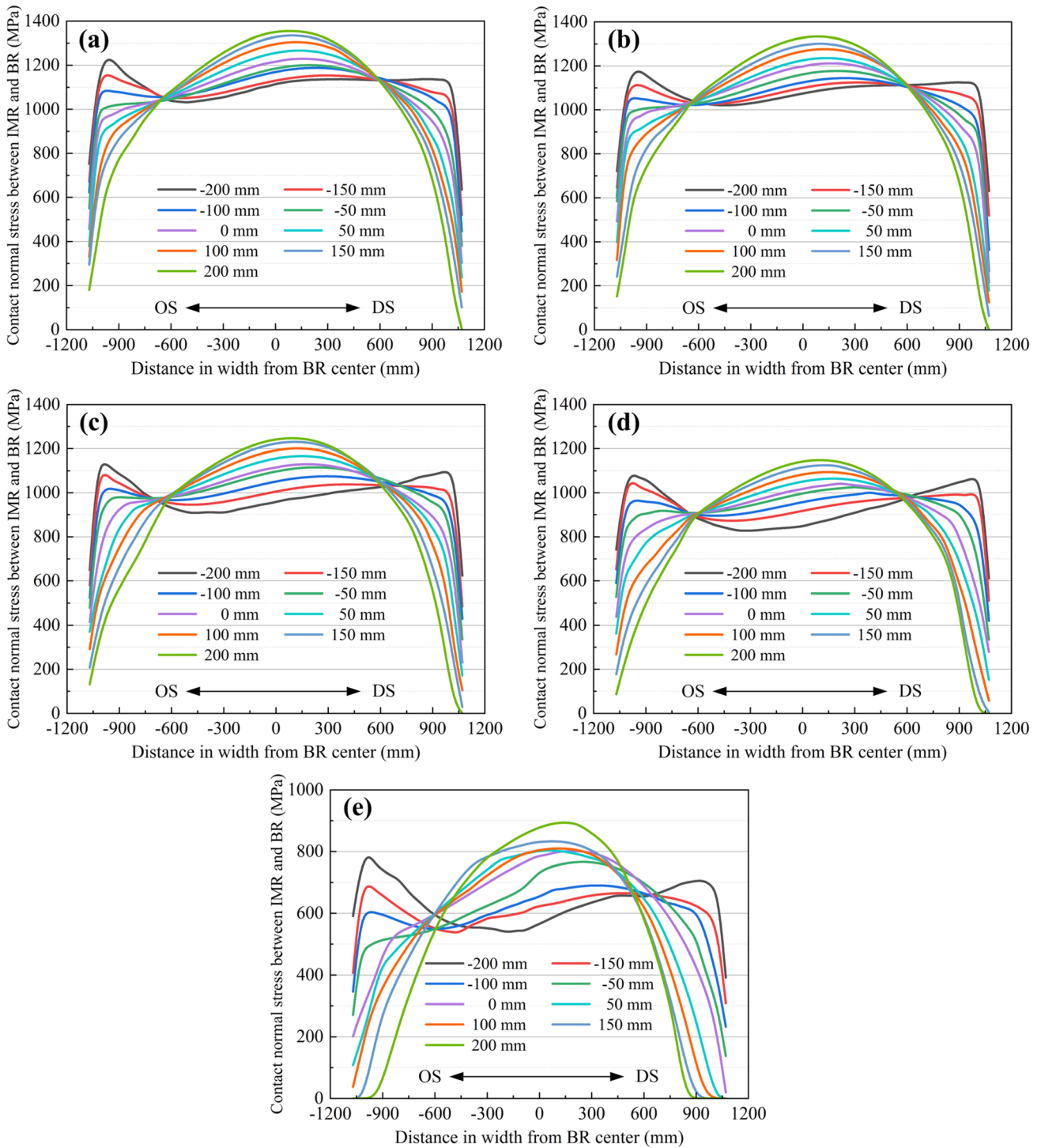
Fig. 18 Contact normal stress between the IMR and BR under different IRSs: **a** S1; **b** S2; **c** S3; **d** S4; **e** S5

6.3 Distribution characteristics of contact normal stress between rolls

From Figs. 16 and 18, it can be seen that when the IRS rises from −200 to 200 mm, there is an increase in the contact normal stress in the roll central region, but a decrease at both roll edges. This finding is consistent with that of Wang et al. [18]. The reason for this result is that: when the IRS increases, the crown of the loaded roll gap profile decreases, which leads to an increase in strip plastic deformation located at
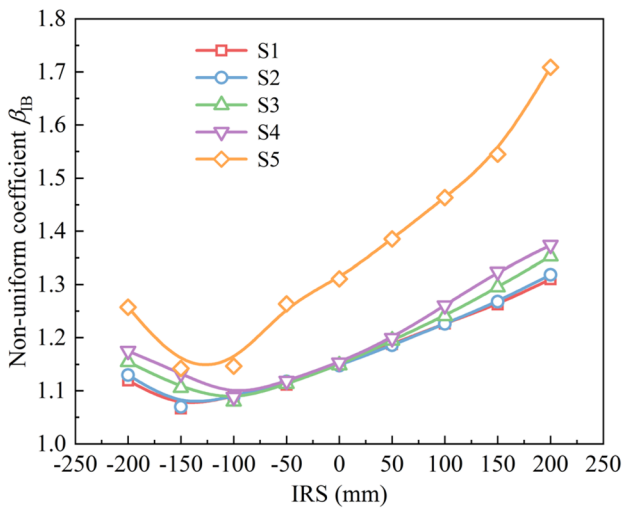
Fig. 19 The non-uniform coefficient β_{IB} under different IRSs from S1 to S5

the strip centre, but a decrease in strip deformation located at the strip edge. As a result, the stress in the roll central region increases, but the stress at the strip edge decreases.

Comparison between Figs. 16 and 18 shows that the maximum contact normal stress between the WR and IMR is larger than that between the IMR and BR at each stand. This result agrees with the finding in [18]. This is attributed to the compatibility of the roll contour. Specifically, as presented in Fig. 1, the WR contour is the conventional contour and the IMR is ground with the CVC contour, so there is an obvious clearance between the contact surfaces of WR and IMR in the initial state, thus causing the high localised peak contact normal stress. By contrast, due to the BR being designed with the reverse-CVC contour, the IMR and BR match perfectly each other, thus resulting in relatively low localised peak contact normal stress.

The nonuniform coefficient has been used to evaluate the distribution of contact normal stress between rolls from S1 to S5, as shown in Figs. 17 and 19. As seen in Fig. 17, the minimum β_{WI} occurs when the IRS is -50 mm at both S1 and

S2, while it occurs when the IRS is 0 mm at S3; by contrast, it appears when the IRS is 50 mm at both S4 and S5. This suggests that the appropriate IRS value is different at each stand in terms of the β_{WI}. Similarly, as illustrated in Fig. 19, when the IRS is -150 mm, the β_{IB} reaches minima at S1, S2 and S5; in comparison, when the IRS is -100 mm, the β_{IB} is at minima at S3 and S4. This implies that the proper IRS value is also different for each stand from the aspect of β_{IB}. These findings have been novelly obtained through using the developed multi-stand FE model. According to the above analysis, it can be concluded that when setting up the IRS value, it not only should meet the target crown and flatness according to the quantitative relationships shown in Figs. 10, 13 and 21, but also there is a need to consider as small β_{WI} and β_{IB} as possible at each stand to alleviate the roll wear.

Moreover, it can also be found in Fig. 17 that the β_{WI} displays an upward trend from S1 to S5 when it comes to the same IRS. The possible explanation for this new finding is that the strip plastic rigidity increases continuously from S1 to S5 (see Fig. 20a), thus leading to an increase in plastic deformation resistance of the strip, which causes more uneven elastic deflection and flattening deformation of rolls. As a result, the contact stress between the WR and IMR is distributed more and more non-uniformly along the roll width direction from S1 to S5. Besides, the β_{IB} shows a similar variation to that of β_{WI}, except that the β_{IB} has almost the same value when it comes to the same IRS (from -100 to 50 mm) from S1 to S4 (see Fig. 19). However, the special phenomenon is difficult to explain clearly based on the current results and theory. This will be studied in future work.

According to the above analyses, it can be concluded that the effect of the IRS on the strip crown, strip flatness, loaded roll gap profile and contact normal stress between rolls were thoroughly analysed at each stand from S1 to S5, and each stand shows significantly different characteristics with various influence factors (see Figs. 11, 14, and 22) and non-uniform coefficients (see Figs. 17 and 19). This differs obviously from previous studies [18, 20–24] using the single stand FE model. More importantly, this study elucidates the nonlinear relationship between the regulation ability of the

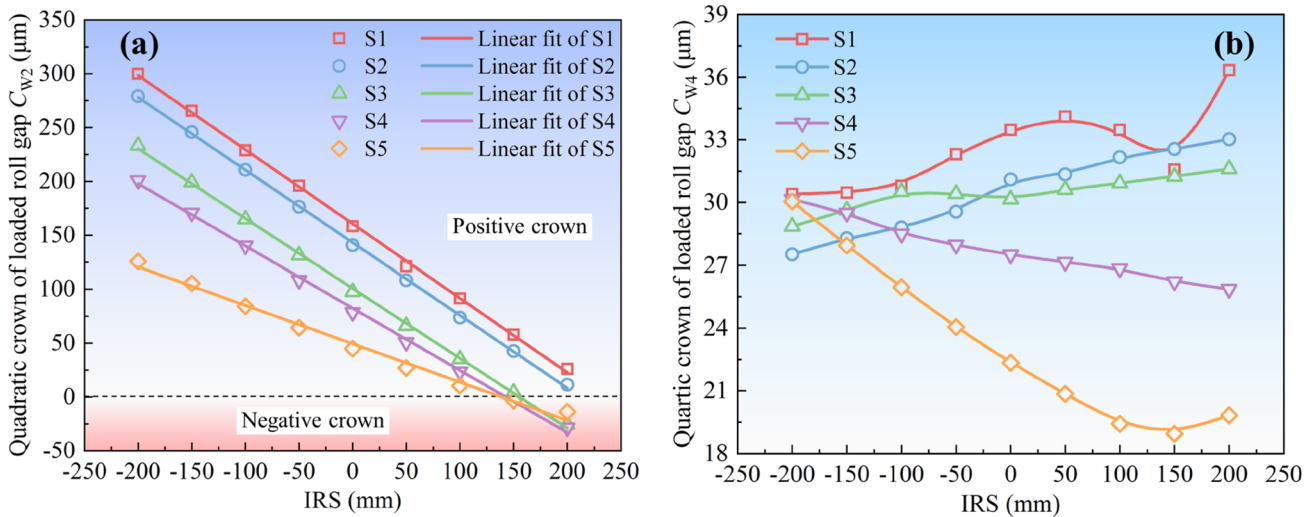**Fig. 20** **a** The Q and K_C from S1 to S5. **b** The curve of K_C–Q
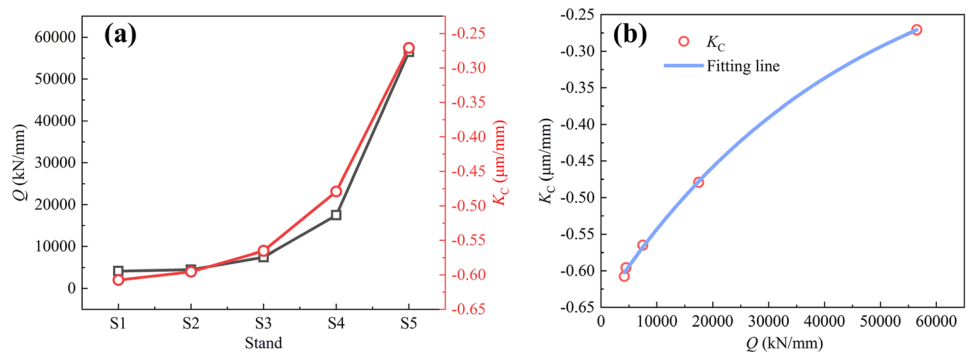
Fig. 21 The crown of the loaded roll gap profile under different IRSs from S1 to S5: **a** C_{W2}; **b** C_{W4}
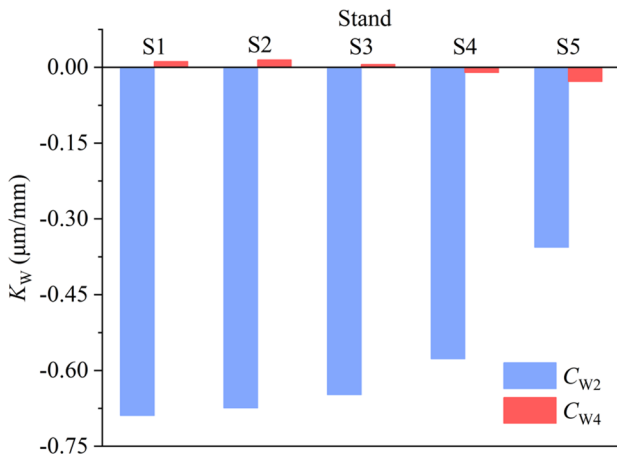

Fig. 22 The efficiency factor of the IRS on the crown of the loaded roll gap profile from S1 to S5

IRS on the strip crown and the strip plastic rigidity (see Fig. 20), which cannot be obtained by employing the single stand FE model. This further demonstrates the superiority and necessity of developing the multi-stand FE model for the TCR.

7 Conclusions

1. With an increase in the IRS at each stand, the strip crown displays a linearly declining trend, but the quadratic flatness shows a linearly rising trend, and the flatness type evolves from the edge wave to the centre wave. However, the IRS has little effect on the quartic flatness.

2. The absolute value of K_C decreases from 0.608 μm/mm at S1 to 0.271 μm/mm at S5. This suggests that the regulation ability of the IRS on the strip crown decreases from S1 to S5. This trend is dependent on the strip plastic rigidity.

3. From S1 to S4, the K_F of quadratic flatness rises from 0.023 to 0.057 IU/mm, and then declines to 0.035 IU/mm at S5. This indicates that the regulation ability of the IRS on the quadratic flatness increases significantly from S1 to S4, but decreases obviously at S5.

4. With an increase in the IRS at each stand, the quadratic crown of the loaded roll gap profile decreases linearly. Furthermore, the absolute value of K_W for the quadratic crown decreases from 0.689 μm/mm at S1 to 0.356 μm/mm at S5, which means that the regulation ability of the IRS on the quadratic crown shows a decreasing trend from S1 to S5. However, the IRS has no obvious influence on the quartic crown of the loaded roll gap profile.

5. With an increase in the IRS at each stand, the contact normal stress between rolls increases in the roll central region, but decreases at both the roll edges. Besides, the least nonuniform stress distribution occurs at different IRSs from S1 to S5, which provides a valuable reference for determining the appropriate IRS value to reduce the roll wear.

Declarations

Ethics approval Not applicable.

Consent to participate Not applicable.

Consent for publication Not applicable.

Conflict of interest The authors declare no competing interests.

References

1. Zhou ZQ, Lam Y, Thomson PF et al (2007) Numerical analysis of the flatness of thin, rolled steel strip on the runout table. Proc Inst Mech Eng B J Eng Manuf 221:241–254
2. Wang QL, Sun J, Li X et al (2020) Analysis of lateral metal flow-induced flatness deviations of rolled steel strip: mathematical modeling and simulation experiments. Appl Math Model 77:289–308
3. He AR, Shao J, Sun WQ (2016) Theory and practice of shape control. Metallurgical Industry Press, Beijing
4. Imai I (1980) New six-high mill (NHM) and automatic shape control system in cold rolling. In: International Conference on Steel Rolling, pp 807–818
5. Nakajima K, Asamura T, Kikuma T et al (1984) Hot strip crown control by six-high mill. Trans Iron Steel Inst Jpn 24:284–291
6. Wang LP, Zhu QY, Zhao HY (2020) Optimization design of a novel X-type six-high rolling mill based on maximum roll system stiffness. PLoS ONE 15:e0228593
7. Ogawa S, Hamauzu S, Matsumoto H et al (1991) Prediction of flatness of fine gauge strip rolled by 12-high cluster mill. ISIJ Int 31:599–606
8. Gunawardene GWDM, Grimble MJ, Thomson A (1981) Static model for Sendzimir cold-rolling mill. Metals Technol 8:274–283
9. Matsumoto H, Tsukamoto H, Hatae S et al (1984) Development of a pair cross rolling mill for crown control of hot strip. Proc Adv Technol Plast 1372–1377
10. Yan ZW, Bu HA, Ma GS et al (2014) Stepped cooling control model based on optimal algorithm. Adv Mater Res 989:2165–2168
11. Bald W, Beisemann G, Feldmann H et al (1987) Continuously variable crown (CVC) rolling. Iron Steel Eng 64:32–41
12. Chen XL, Yang Q, Zhang QD et al (1995) Varying contact backup roll for improved strip flatness. Steel Technol Int 174–178
13. Seilinger A, Mayrhofer A, Kainz A (2002) SmartCrown - a new system for improved profile and flatness control in rolling mills. Iron Steel Rev Int 46:84–88
14. Kitamura K, Yarita I, Suganuma N et al (1992) Edge-drop control of hot and cold rolled strip by tapered-crown work roll shifting mill. Kawasaki Steelmaking Tech Rep 27:5–12
15. Jiang ZL, Wang GD, Zhang Q et al (1993) Shifting-roll profile and control characteristics. J Mater Process Technol 37:53–60
16. Lu C, Tieu AK, Jiang ZY (2002) A design of a third-order CVC roll profile. J Mater Process Technol 125–126:645–648
17. Xu JZ, Gong DY, Jiang ZY et al (2012) Mechanics of design and model development of CVC-plus roll curve. Adv Mater Res 418:1158–1166
18. Wang QL, Li X, Sun J et al (2021) Mathematical and numerical analysis of cross-directional control for SmartCrown rolls in strip mill. J Manuf Process 69:451–472
19. Ding JG, He YHC, Song MX et al (2021) Roll crown control capacity of sextic CVC work roll curves in plate rolling process. Int J Adv Manuf Technol 113:87–97
20. Sun JN, Du FS, Li XT (2008) FEM simulation of the roll deformation of six-high CVC mill in cold strip rolling. In: Zhu JR (ed) 2008 International Workshop on Modelling. Simulation and Optimization, Hong Kong, pp 412–415
21. Linghu KZ, Jiang ZY, Zhao JW et al (2014) 3D FEM analysis of strip shape during multi-pass rolling in a 6-high CVC cold rolling mill. Int J Adv Manuf Technol 74:1733–1745
22. Li HB, Zhao ZW, Zhang J et al (2018) Analysis of flatness control capability based on the effect function and roll contour optimization for 6-h CVC cold rolling mill. Int J Adv Manuf Technol 100:2387–2399
23. Wang QL, Sun J, Liu YM et al (2017) Analysis of symmetrical flatness actuator efficiencies for UCM cold rolling mill by 3D elastic–plastic FEM. Int J Adv Manuf Technol 92:1371–1389
24. Wang QL, Li X, Hu YJ et al (2018) Numerical analysis of intermediate roll shifting-induced rigidity characteristics of UCM cold rolling mill. Steel Res Int 89:1700454
25. Wang XC, Yang Q, He HN et al (2020) Effect of work roll shifting control on edge drop for 6-hi tandem cold mills based on finite element method model. Int J Adv Manuf Technol 107:2497–2511
26. Li LJ, Xie HB, Liu TW et al (2021) Effects of rolling force on strip shape during tandem cold rolling using a novel multistand finite element model. Steel Res Int 93:2100359
27. Li LJ, Xie HB, Liu TW et al (2022) Numerical analysis of the strip crown inheritance in tandem cold rolling by a novel 3D multistand FE model. Int J Adv Manuf Technol 120:3683–3704
28. Zhang SH, Deng L, Tian WH et al (2022) Deduction of a quadratic velocity field and its application to rolling force of extra-thick plate. Comput Math Appl 109:58–73
29. Zhang SH, Deng L, Che LZ (2022) An integrated model of rolling force for extra-thick plate by combining theoretical model and neural network model. J Manuf Process 75:100–109
30. Cao JG, Chai XT, Li YL et al (2018) Integrated design of roll contours for strip edge drop and crown control in tandem cold rolling mills. J Mater Process Technol 252:432–439
31. Yang GH, Zhang J, Cao JG et al (2015) Strip shape control and inspection in tandem cold rolling. Metallurgical Industry Press, Beijing

32. Grimble M, Fotakis J (1982) The design of strip shape control systems for Sendzimir mills. IEEE Trans Autom Control 27:656–666

33. Judin M, Nylander J, Larkiola J et al (2011) Quality parameters defined by Chebyshev polynomials in cold rolling process chain. In: Menary G (ed) The 14th International ESAFORM Conference on Material Forming: ESAFORM 2011. American Institute of Physics, Belfast, pp 368–373